applied sciences

MDPI

Article

Anisotropy and Directivity Effects on Uniaxial Compression of Carbonaceous Slate Form Jinman Mine

Zhixiong Zhang [1,2], Yun Cheng [3,*], Zhanping Song [4,*] and Xueyun Ye [5]

[1] College of Civil Engineering and Architecture, Beibu Gulf University, Qinzhou 535011, China
[2] Key Laboratory of Beibu Gulf Offshore Engineering Equipment and Technology, Beibu Gulf University, Qinzhou 535011, China
[3] School of Civil Engineering, Yancheng Institute of Technology, Yancheng 224051, China
[4] School of Civil Engineering, Xi'an University of Architecture and Technology, Xi'an 710055, China
[5] College of Electronic and Information Engineering, Beibu Gulf University, Qinzhou 535011, China
* Correspondence: chengyun@xauat.edu.cn (Y.C.); songzhpyt@xauat.edu.cn (Z.S.); Tel./Fax: +86-1738-920-6265 (Y.C.); +86-1318-608-8693 (Z.S.)

Abstract: To determine the anisotropic mechanical characteristics of carbonaceous slate at the Jinman Mine located in Lancang River Gorge, China, uniaxial compression, acoustic emission (AE) monitoring, and scanning electron microscopy (SEM) tests were conducted. The results show that stress loading directions and bedding effects have a significant impact on strain characteristics. The deformation of slate undergoes compaction, elastic, damage accumulation, and failure stages, and there are significant differences in strain paths. The mechanical properties of grey and carbonaceous slate have significant features, and variations of these properties of carbonaceous slate are more than that of grey slate. The discrete degree is significantly related to the direction of stress loading and different types of slate structures. The AE response intensity is related to the loading mode and slate type. A sudden increase in the AE cumulative ring number near peak stress indicates instability and rupture and is a precursor of rock rupture. The failure patterns and fracture characteristics are significantly correlated to the layered structure of the slate. Slates subjected to vertical loading and parallel loading conditions are dominated by shear fracture and tensile fracture, respectively. The peak strains of gray and carbonaceous slate correspond to brittle failure. The SEM tests indicate that slate samples subjected to parallel loading primarily show a tensile failure compared with slate samples subjected to vertical loading, with fractured sections being of lesser roughness, and scattered fractures and sections being smooth without obvious protrusions or cracks.

Keywords: carbonaceous slate; anisotropic mechanical characteristics; failure patterns; scanning electron microscope; acoustic emission characteristics

Citation: Zhang, Z.; Cheng, Y.; Song, Z.; Ye, X. Anisotropy and Directivity Effects on Uniaxial Compression of Carbonaceous Slate Form Jinman Mine. *Appl. Sci.* **2022**, *12*, 9811. https://doi.org/10.3390/app12199811

Academic Editor: Muhammad Junaid Munir

Received: 16 September 2022
Accepted: 28 September 2022
Published: 29 September 2022

1. Introduction

With the gradual implementation of a deep exploitation strategy, the geotechnical engineering field has been demanding space resources from deep rock mass [1–4]. In 1991, the Tokyo Declaration was adopted after the International Academic Conference on the Utilization of Urban Underground Space held in Tokyo proposed that the 21st Century would be the century for the development and utilization of underground space [3,5–7]. Weak metamorphic rocks such as slate, phyllite, and schist are widely distributed in northwestern the Yunnan Province in China. The presence of rich mineral resources such as copper, lead, zinc, and silver has resulted in the mining of these resources, which has been associated with frequent accidents. Slate rock is a type of metamorphic rock that is widely distributed in northwestern Yunnan. There are a large number of weak structural surfaces such as fractures, slabs, and bedding that are composed of clay minerals. The fillers near the structural surface are composed of mineral particles with cohesion and strength that are lower than that of intact rock, which causes the physical and mechanical properties of

slate to have significant anisotropy. Hence, isotropic assumptions are used for calculating the stability of stope overestimate the bearing capacity of surrounding rock.

With the rapid development of underground engineering [8–11], a substantial amount of data is now available for the study of rock anisotropy. Vervoort et al. [12] studied the anisotropic behavior of tensile strength and fracture mode of Mosel slate, Postaer sandstone, and Boryeong shale. Dan and Konietzky [13] analyzed the different characteristics of the variations of mechanical parameters of layered rocks. Zhang et al. [14] found that the acoustic emission event rate and dominant frequency of layered rocks showed anisotropy. Wang et al. [15] found that slate bedding is an important cause of anisotropy of mechanical parameters and fracture modes. Li et al. [16] studied the anisotropic characteristics of silty slate. In addition, some researchers have studied the anisotropy of the Wudang group schist, phyllite. Hou et al. [17] conducted microanalysis to explore anisotropic behavior associated with the fracture morphology of marble. Fan et al. [18] studied the macro-mechanical behavior of jointed rock masses. To study the micro-mechanical characteristics of rocks, Akbarimehr et al. [19] conducted related scanning electron microscopy (SEM) experiments. The above analysis shows that the rock bedding, fragments, and faults cause large differences in the mechanical properties of complete blocks, but the natural anisotropy has not been considered while testing for usual rock strength, such as for compression, tensile, and shear tests. The results of rock mechanics tests show that physical and mechanical properties have a significant anisotropy. Even for rock masses retrieved from the same location, the strength for different directions of stress loading often show differences of 1 to 2 orders of magnitude. Therefore, if mechanical parameters of engineering rock are calibrated under the assumption that natural rock, especially highly weathered slates, are isotropic then such data are not suitable for engineering applications. Hence, it is necessary to consider the natural discrete characteristics of various mechanical parameters, which is of great significance in revealing anisotropic characteristics after transformations, such as joints, fragments, fractures, etc. that are caused by excavation-related unloading [20,21].

The Jinman mine is located in the Lancang River Gorge in Lanping County of theYunnan province. Field investigations have found that carbonaceous slates in roadways show floor heave and slabbing failure. The fracture characteristics of slate rock masses of different colors are significantly different. To investigate the anisotropic mechanical characteristics of carbonaceous slate considering the directivity effect, uniaxial compression tests, acoustic emission (AE) monitoring, and SEM tests were conducted with vertical loading and parallel loading on slate structures. The objectives were: (a) to obtain the characteristic stress-strain curves, (b) to investigate the characteristics of mechanical parameters, (c) to investigate AE characteristics, and (d) to determine failure patterns and fracture characteristics including macro-fracture modes and micro-cracks.

2. Methods

2.1. Sample Preparation

Figure 1 shows the sampling location, partial slate samples, and the mineral contents of rock samples. The carbonaceous slate samples were obtained from the Jinman Mine in Lancang River Gorge in Lanping County, Yunnan Province. The sampling location was located in the secondary overturned anticline of Enqi Anticlinorium as shown in Figure 1a. Affected by geological tectonics, carbonaceous slates in this area have been impacted by floor heave and slabbing failure. From X-ray diffractometer analysis, gray slate is composed of quartz (71%), muscovite (15%), albite (11%), graphite (3%), while cinerous slate is composed of quartz (55%), muscovite (19%), albite (15%), calcium (8%), and graphite (3%), as shown in Figure 1c,d. The average dry density and average longitudinal wave velocity of slate is 2.68 g/mm^3 and 6.49 km/s, respectively.

Cuboid samples of size 50 mm × 50 mm × 100 mm were used for uniaxial compression tests per the Code for Rock Tests of Hydroelectric and Water Test Conservancy Engineering (GB/T50266-2013), as shown in Figure 1b. The relationship between bedding structure and loading direction was controlled to study anisotropic mechanical properties. The loading

methods were such that the principal stress was perpendicular to the slate structure for vertical loading, and the principal stress was parallel to the slate structure for parallel loading. A total of 36 rock samples including 18 gray samples and 18 cinerous samples were used for this study.

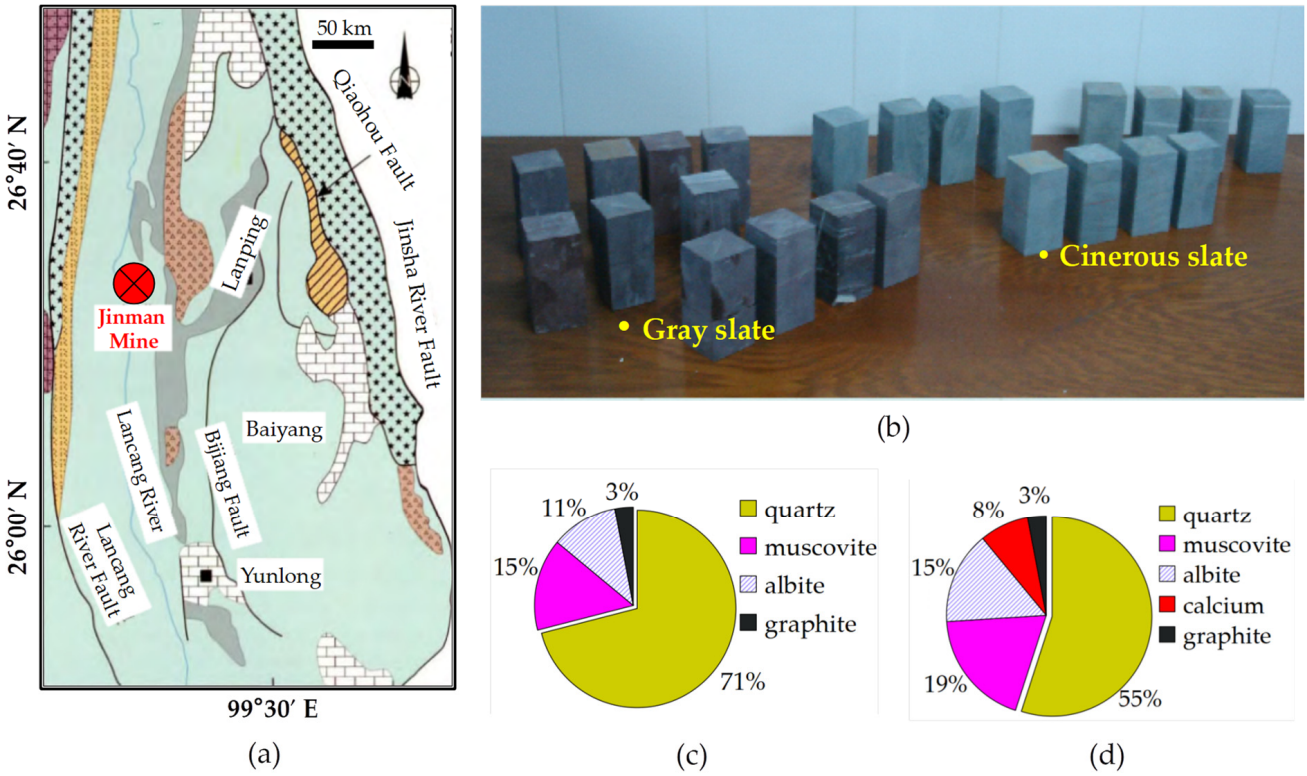

Figure 1. Partial slate samples and mineral contents: (**a**) Jinman Mine [9]; (**b**) Partial slate samples; (**c**) Mineral contents of gray slate; (**d**) Mineral contents of cinerous slate.

2.2. Experimental Apparatus

Heterogeneous mechanical loading tests on slate samples were conducted at Kunming University of Science and Technology. The experimental system of slate mechanics is shown in Figure 2a, which is mainly composed of a mechanical testing machine, a dynamic strain meter, a data display, and storage equipment. A stress-strain data coupling system was designed taking into account the cubic shape of the rock sample with strain gauges capturing strain data, as shown in Figure 2b. The feasibility and reliability of the coupling system were verified in previous studies [22]. The coupling system imports axial stress-time data and strain-time data into the UA304 external parameter collector in real-time, and then processes it based on the SDAES data coupling system provided by Beijing Shenghua Xingya Technology Co., Ltd., Beijing, China to obtain the stress-strain curve.

The maximum loading stress of the mechanical testing machine used for this study is 1100 kN, which can achieve a constant pressure testing function. The load and deformation were measured by stress sensors and resistance strain gauges, respectively. The data collection equipment used was the SDY2107A dynamic strain meter manufactured by Beidaihe Electronic Equipment Co., Ltd. Its gauge factor and sensitivity were 2.00 k and 0.0001 V/με, respectively. The data display equipment used was a DL850E oscillograph manufactured by Yokowaga, Japan, with a resolution and testing range of 12-bit and 0.01~500,000 Hz, respectively. The resistance value, size, power supply voltage, sensitivity factor, and strain limit of resistance strain gauges were 120 ± 1 Ω, 8 mm × 5 mm, 3~10 V, 2.00%, and 20,000 μm/m, respectively.

(**a**)

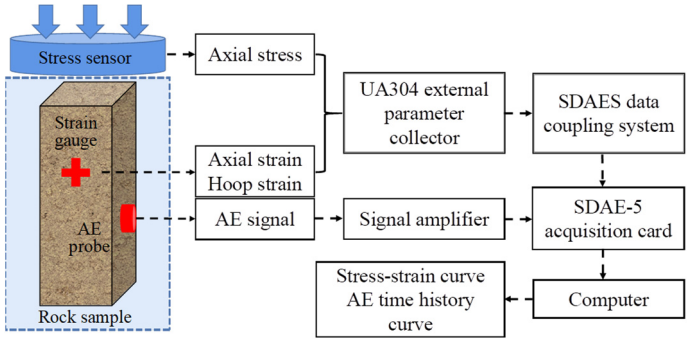

(**b**)

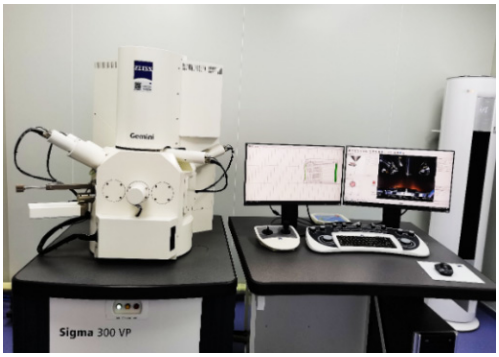

(**c**)

Figure 2. Experimental system: (**a**) Experimental apparatus; (**b**) Stress-strain data coupling system; (**c**) Zeiss ZEISS-SIGMA 300 field emission SEM.

The SEM tests of fracture morphology of slate samples were conducted at the Analysis and Testing Center of Northwest University College of Chemistry and Material Science. The micro-test equipment used was Zeiss ZEISS-SIGMA 300 field emission SEM as shown in Figure 2c. The scanning electron microscope combines performance analysis with field emission scanning technology to generate images of micro-structures of mineral particles and fracture surfaces. The scanning rate was 1 nm@30 kV STEM with a magnification of 10~1,000,000× and a storage resolution of 32 k × 24 k pixels. The AE signals were collected during the destruction process by the SAEU-1016-4 AE instrument, with a maximum acquisition frequency and acquisition precision of 10 MHz and 16-bit, respectively.

2.3. Experimental Procedure

The experimental procedure was as follows: (1) The surfaces of slate samples were polished and cleaned, following which the strain gauges were pasted as shown in Figure 3. The direction of strain gauge 1 was consistent with the principal stress loading direction to obtain axial strain ε_{zz}. The directions of strain gauges 2 and 3 were perpendicular to the

principal stresses to obtain hoop strains ε_{xx} and ε_{yy}. (2) The vertical loading and parallel loading methods are shown in Figure 3. A preload stress of 0.30 kN was applied to ensure good contact between stress sensors and rock samples. The loading method was stress controlled, and the loading rate of principal stress was 0.50 MPa/s until the rock samples showed unstable failure. (3) The stress-strain and acoustic emission data were saved and analyzed, and the fracture types and fragment numbers were counted. Thereafter, SEM tests were conducted on the failure rock blocks to explore the distinguishing shape characteristics of fracture morphology.

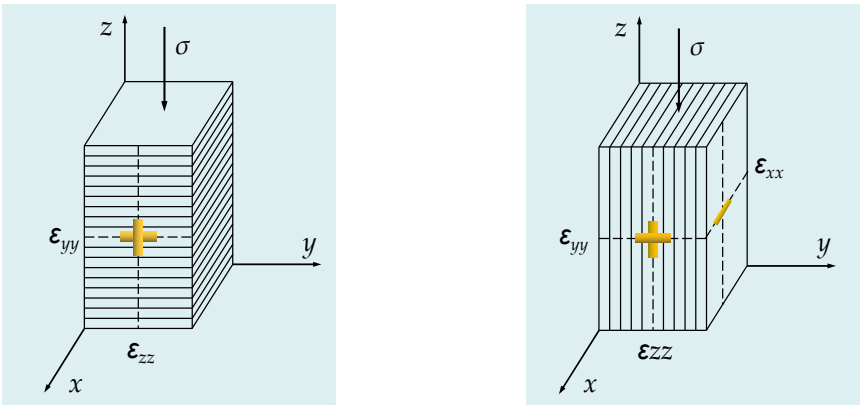

Figure 3. Stress loading method: (**a**) Vertical loading; (**b**) Parallel loading.

3. Results and Discussion

3.1. Effect of Rock Structure on Stress-Strain Curves

The repeatability of experimental results allows the use of experimental outcomes for engineering applications. To evaluate the repeatability of experimental results of samples containing different rock structures, four identical samples of each formation were prepared and subjected to the same loading conditions. Figures 4 and 5 show the typical stress-strain curves including axial stress-strain curve (σ-ε_{xx}), hoop stress-strain curve (σ-ε_{xx}, σ-ε_{yy}), and volumetric stress-strain curve (σ-ε_v) for vertical loading and parallel loading of gray and cinerous samples. The structural deformations of horizontal rock layers were similar to vertical loading conditions, and we only tested the hoop stress-strain curve (σ-ε_{yy}). It is observed that the stress-strain curves for different loading conditions can be divided into the initial compaction stage (stage I), elastic deformation stage (stage II), and damage accumulation stage (stage III), as shown in Figures 4 and 5.

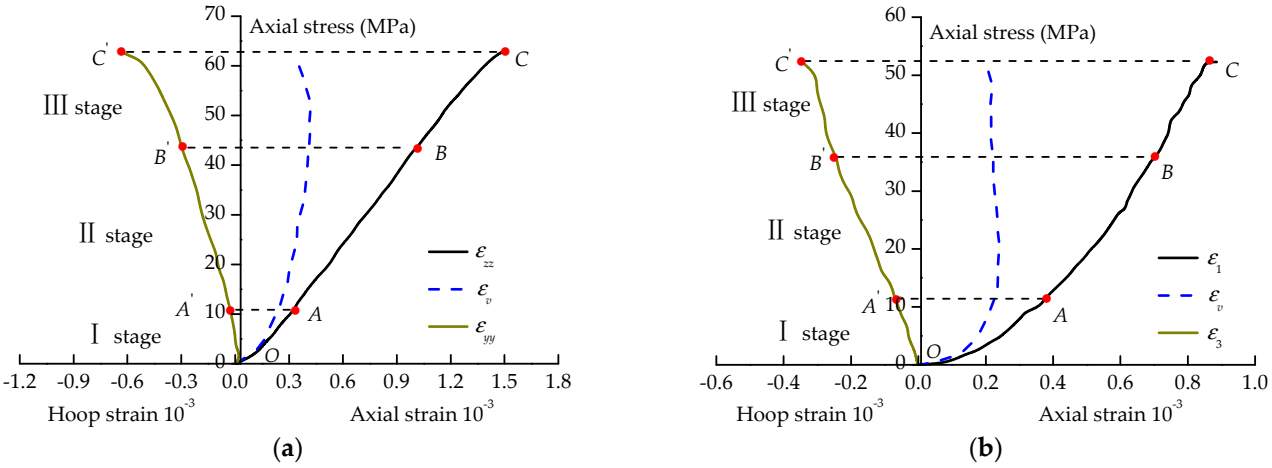

Figure 4. Stress−strain curves under vertical loading: (**a**) Gray samples; (**b**) Cinerous samples.

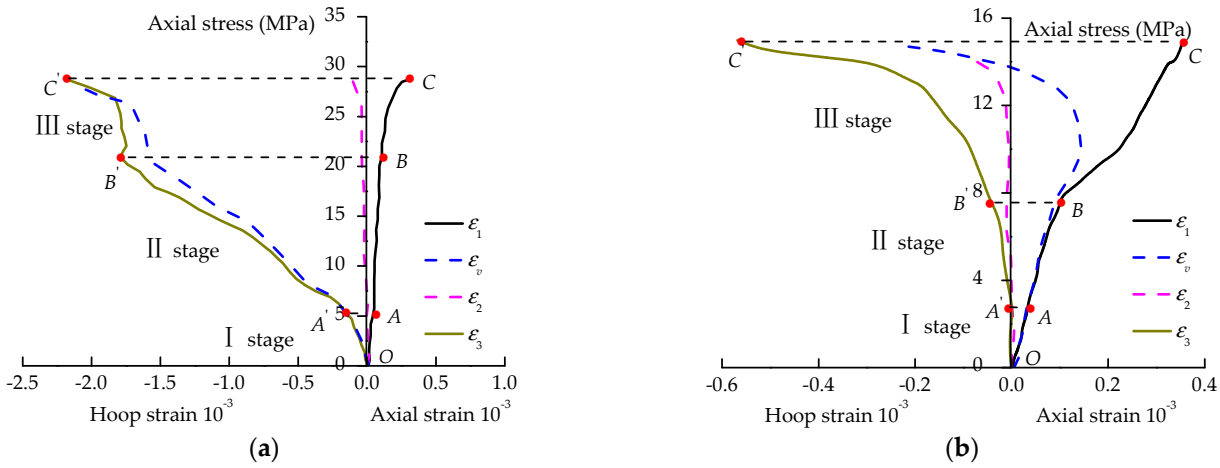

Figure 5. Stress−strain curves under parallel loading: (**a**) Gray samples; (**b**) Cinerous samples.

The initial compaction stage (stage I) shows that the axial deformations for both vertical loading and parallel loading are similar. When the vertical stress was loaded, the slate sample was compacted by a small load due to many micropores among the weak surface structures. The vertically superimposed slate rock had a rock pillar effect during parallel loading [17]. The strength of natural slate is noticeably greater than the strength of bedding cementation. The superimposed slate rock may only undergo axial compression and an adjustment of the alignment of mineral bundles due to a small axial loading, but not show a significant compaction process similar to that due to vertical loading.

The slate samples enter the elastic deformation stage (stage II) after the completion of existing micro-fractures and cementation compaction with further loading of axial stress. Thereafter, the integral rigidity increases and the stress-strain curve increases approximately linearly. The gray and cinerous samples show linear deformation when the load is perpendicular to the weak surface structures; axial compression controls the overall deformation, and the axial deformation is about 1.50 to 2.50 times that of hoop deformation, as shown in Figure 4. The rock pillar formed by superimposition is sufficient to support the axial load when the load is parallel to weak surface structures; the relative axial strain of gray slate and cinerous slate is smaller than the vertical loading condition, as shown in Figure 5. Tables 1 and 2 show that the average elastic modulus of the cinerous samples is significantly greater than that of the gray samples for both vertical and parallel loading. This is because the weak surfaces of the slate rock layers and main stresses are related in series during vertical loading, and slate rock is dominated by compression deformation while hoop deformation is constrained.

Table 1. Mechanical parameters for vertical loading.

Sample	σ_c/MPa	σ_{cd}/MPa	*E*/MPa	$\varepsilon_{zz} \times 10^{-3}$	$\varepsilon_{yy} \times 10^{-3}$	$\varepsilon_v \times 10^{-3}$
No. 1 Gray sample	63.27	50.26	35.11	1.802	−0.290	1.222
No. 2 Gray sample	61.63	49.63	43.01	1.433	−0.561	3.110
No. 3 Gray sample	45.02	39.02	36.39	1.237	−0.254	0.727
No. 4 Gray sample	63.45	51.45	41.35	2.972	−0.517	1.938
Average	58.34	47.59	38.97	1.861	−0.406	1.749
No. 1 Cinerous sample	22.41	19.41	32.02	1.365	−0.114	1.137
No. 2 Cinerous sample	53.93	30.77	32.49	2.047	−0.169	0.609
No. 3 Cinerous sample	70.19	68.19	64.34	1.091	−0.204	0.683
No. 4 Cinerous sample	69.17	57.55	38.06	1.373	−0.930	0.487
Average	53.93	43.98	41.72	1.469	−0.354	0.927

Table 2. Mechanical Parameters for Parallel Loading.

Sample	σ_c/MPa	σ_{cd}/MPa	E/MPa	$\varepsilon_{zz} \times 10^{-4}$	$\varepsilon_{xx} \times 10^{-3}$	$\varepsilon_{yy} \times 10^{-3}$	$\varepsilon_v \times 10^{-3}$
No. 1 Gray sample	53.26	39.03	40.55	3.27	−0.061	−0.886	−0.620
No. 2 Gray sample	55.43	43.56	88.55	6.26	−0.570	−2.691	−2.635
No. 3 Gray sample	47.95	28.99	54.70	5.11	−0.623	−2.879	−2.991
No. 4 Gray sample	34.15	29.52	41.14	5.78	−0.071	−0.670	−0.163
Average	47.70	35.28	56.24	5.11	−0.331	−1.782	−1.602
No. 1 Cinerous sample	54.88	48.89	41.11	1.44	−0.035	−3.507	−3.398
No. 2 Cinerous sample	28.92	23.73	62.08	1.50	−0.087	−3.182	−3.119
No. 3 Cinerous sample	50.52	46.38	78.28	1.58	−0.020	−1.892	−1.854
No. 4 Cinerous sample	12.98	8.64	50.62	1.29	−0.015	−1.254	−1.140
Average	36.83	31.91	58.02	1.45	−0.039	−2.459	−2.378

The stress-strain curves in the damage accumulation stage (stage III) demonstrate an increase in yield after elastic deformation due to the expansion of partial pores caused by compression. The stress concentration between weak surfaces leads to an accumulation of damage to the rock samples, which intensifies the propagation of new fragments [15,16]. The overall stiffness is gradually reduced due to an increase in the deterioration degree of rock samples. There is a significant difference in the yield shape of stress-strain curves between vertical loading and parallel loading, which is related to the difference in the structural expansion mechanism of slate samples. The low bedding cohesion causes the fragments and original defects to quickly penetrate when the load is parallel to weak surface structures, which is manifested as the rapid development of damage deformation. The superimposed slate is segregated into thin slices and the slate samples with lower strength show buckling failure [23]. Significant lateral deformation causes the volumetric stress-strain curve to deviate from the original development trajectory, resulting in multiple inflection points. The hoop deformation due to parallel loading is greater than the axial deformation due to further increases in axial stress. A weak surface structure gradually plays a leading role in the overall deformation, and the rock body shows a significant expansion [24]. However, the yield deformation curve due to vertical loading has a trend opposite that of parallel loading.

In this study the slate samples entered a failure stage as the axial stress was increased significantly. The internal cracks gradually penetrated and began to rupture. Cracks developed rapidly to form macroscopic fracture surfaces, the rock samples showed structural dislocation, and the bearing capacity of the samples decreased rapidly. The strain gauges underwent sudden failure and were therefore unable to obtain post-peak stress-strain data. Therefore, only the pre-peak stress-strain curves could be obtained from the stress-strain data coupling system.

3.2. Loading Effect of Mechanical Parameters

The bedding effect and stress loading directions of the slate samples have a significant effect on the deformation and damage evolution characteristics. To quantify the deformation characteristics, Tables 1 and 2 show the peak strength (σ_c), expansion strength (σ_{cd}), elastic modulus (E), axial peak strain (ε_{zz}), hoop peak strain (ε_{xx} and ε_{yy}), and volume peak strain (ε_v) for vertical loading and parallel loading.

3.2.1. Effect of Slate Structure on Peak Strength

The peak strength for vertical loading and parallel loading conditions were evaluated based on the results of uniaxial compression tests of different slate samples as shown in Figures 4 and 5. As observed in Table 1, the overall rock structure stability is relatively high due to the series relationship of the slate structure due to vertical loading. The peak strength of the gray samples at fracture is 45.02–63.45 MPa and the average peak strength is 58.34 MPa. The peak strength of the cinerous samples is 22.41–70.19 MPa, with an average peak strength of 53.93 MPa which is approximately 92.44% of gray samples. The expansion

strength of the slate samples in the yield deformation stage shows a similar variation, i.e., the greater the peak strength, the greater the expansion strength. The expansion strength of the cinerous samples is approximately 92.41% of that of gray samples. This indicates that the cinerous samples underwent dilation and rupture earlier in the yield deformation stage than the gray samples under vertical loading conditions, which is related to the physical properties of the diagenesis effect [24,25].

The slate structures changed from a series relationship to a parallel relationship when the slate samples were subjected to parallel loading. The superimposed action of the slate strata caused the rock samples to exhibit a rock column effect [22,25,26]. The rock samples exhibited significant expansion deformation due to the tensile deformation of weak bedding surface, and the bearing capacity was significantly deteriorated compared with the vertical loading condition. A buckling failure occurred near the peak strength due to insufficient bearing capacity [27]. Table 2 shows that under parallel loading conditions, the peak strength of the gray samples at brittle fracture is 34.15–55.43 MPa with an average peak strength of 47.70 MPa, which is reduced by 18.24% compared with vertical loading. The peak strength of cinerous samples at brittle fracture is 13.98–54.88 MPa, and the average peak strength is 36.83 MPa, which is 31.70% lower than that for vertical loading.

The expansion strength of slate samples also deteriorated significantly as shown in Tables 1 and 2, the expansion strength of the gray samples and the cinerous samples with yield deformation decreased by 25.87% and 27.44%, respectively, compared with the expansion strength under vertical loading conditions. It can be seen that the slate peak strength and expansion strength are consistently correlated with the slate structure, i.e., the greater the bearing strength, the greater the expansion strength of the slate sample in yield deformation. The parallel loading condition was the primary reason for the roadway failure in the Jinman mining area.

3.2.2. Effect of Slate Structure on Elastic Modulus

The elastic modulus is another important engineering parameter that characterizes the mechanical properties of slate samples. Tables 1 and 2 show the distribution characteristics of the elastic modulus of slate samples for different loading conditions, which demonstrates the effect of slate structure on elastic modulus. The elastic modulus of the gray samples under vertical loading is 35.11–43.01 MPa, and the average elastic modulus is 38.97 MPa. The elastic modulus of the cinerous samples is 16.02–64.34 MPa, and the average elastic modulus is 37.73 MPa, which is slightly smaller than that of gray samples. This shows that the gray samples have stronger elastic deformation, which is consistent with the variation of peak strength.

The slate stratum structure under parallel loading conditions shows a parallel relationship with the principal stress, and the slate structure plays a major bearing role on the slate rock. The slate samples had significant expansion deformation while the compression deformation was relatively restricted. This resulted in a steeper linear growth of the stress-strain curve and the elastic deformation was relatively intensified. As presented in Tables 1 and 2, the elastic moduli of gray samples and cinerous samples are 41.44–88.55 MPa and 41.11–78.28 MPa, respectively, and their average elastic modulus fractions are 56.24 MPa and 58.02 MPa, respectively, which are 1.44 times and 1.54 times higher than those under vertical loading, respectively. It can be seen that although the slate structure has a significant cracking effect on the bearing strength of slate rock, it has a certain strengthening effect on the elastic deformation.

3.2.3. Characteristics of Mechanical Parameters

The above analysis shows that the uniaxial compression mechanical properties of gray slate and cinerous slate have certain discrete characteristics. The concept of variation coefficient [16] is introduced to describe the characteristics of carbonaceous slate and is defined as the ratio of the mechanical parameters of parallel bedding and vertical bedding for the same stress loading state. Based on the peak strength (σ_c), expansion strength (σ_{cd}),

and elastic modulus (E), the variation coefficient (K) is defined by the following equation, where 'par' indicates that the loading stress is parallel to the slate structure, and 'var' indicates that the loading stress is perpendicular to the slate structure.

$$K = \frac{\psi_{ver}}{\kappa_{par}}$$

Figure 6 shows the variation coefficients of the slate samples based on the above equation. The variation coefficient of gray slate samples is characterized by peak stress (σ_c), expansion stress (σ_{cd}), and elastic modulus (E) of 1.22, 1.35, and 0.69, respectively. The variation coefficient of the carbonaceous slate samples is characterized by peak stress (σ_c), expansion stress (σ_{cd}), and elastic modulus of 1.46, 1.38, and 0.71, respectively. The above analysis shows that the uniaxial compression mechanical properties of gray and cinerous slate under different loading conditions have significant and discrete characteristics. The variations of carbonaceous samples are greater than those of gray samples, and they show complex fracture patterns and uneven fracture patterns in macroscopic views. The discrete degree is significantly related to the direction of stress loading and different types of slate structures.

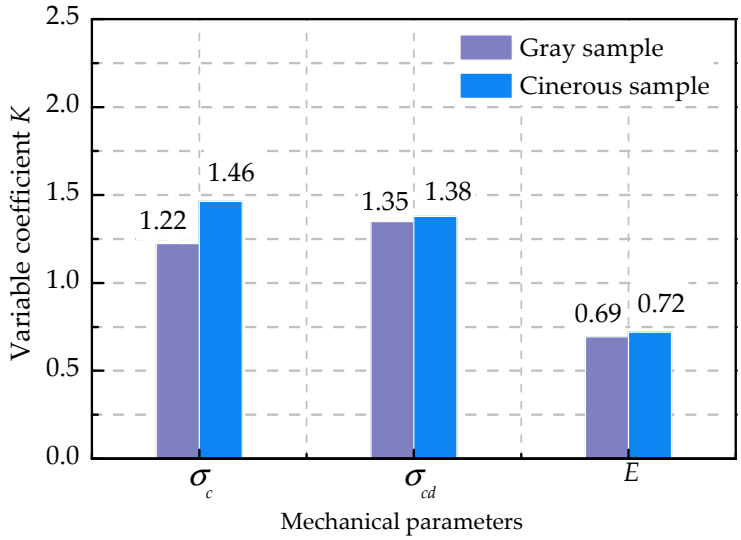

Figure 6. Variation coefficients of slate samples.

Analysis of the slate structural features shows that there are differences in the appearance and morphology of slate samples. Gray slate alternates with being gray and white, with a good filling and adhesive bonding in the bedding. The appearance of carbonaceous slate is uniform in color, but the slate structure is weak. The structural surface has muddy fillings, and the distribution of mineral composition and original fractures are quite different, showing complex fracture modes and uneven fracture morphology at the macro level. The superimposed structural characteristics of slate samples show that the discrete characteristics of mechanical parameters are also related to the distribution characteristics of macroscopic joints. The directionality of the cleat system restricts the anisotropy of the mechanical properties. Different stress loading directions and complex bedding superimposed structures are the external and internal reasons for the variability of slate mechanical characteristics.

3.3. Acoustic Emission Response Characteristics

Acoustic emission (AE) is the phenomenon of generating transient elastic waves during compression of rock, accompanied by external energy input and rapid release of strain energy [25,28]. The AE cumulative ring number can directly reflect the structural

reorganization and redistribution of stress within a rock sample, thereby revealing the failure mechanism of slate. Figures 7 and 8 show the corresponding relationships between the AE cumulative ring number and axial stress of slate samples. The AE cumulative ring number is consistent with axial stress and is roughly similar to the evolutionary process of a quiet stage (stage I), a rapid increase stage (stage II), and a sudden increase stage (stage III).

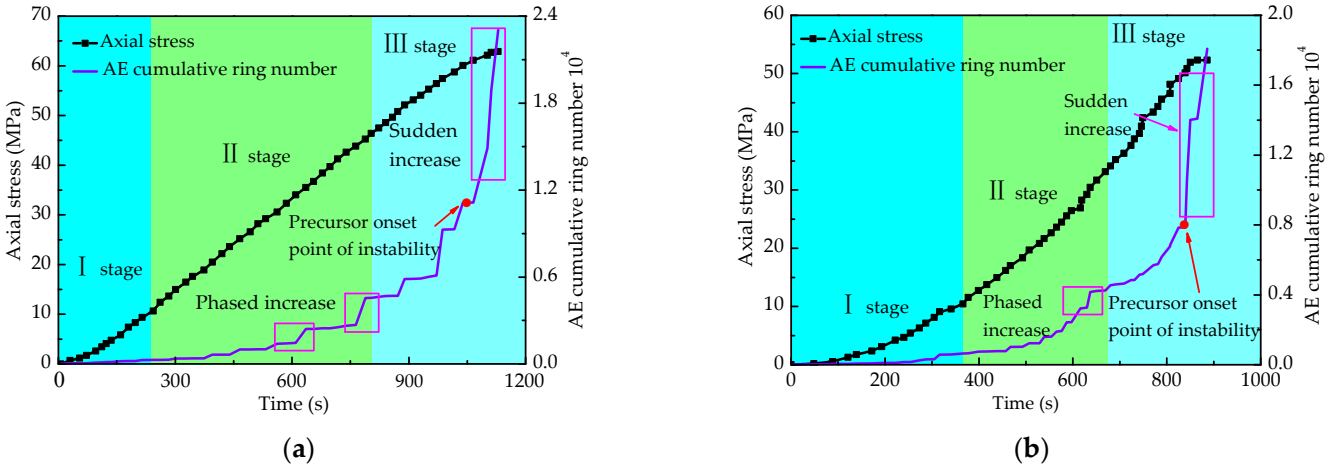

Figure 7. Evolution of AE cumulative ring number under vertical loading: (**a**) Gray samples; (**b**) Carbonaceous samples.

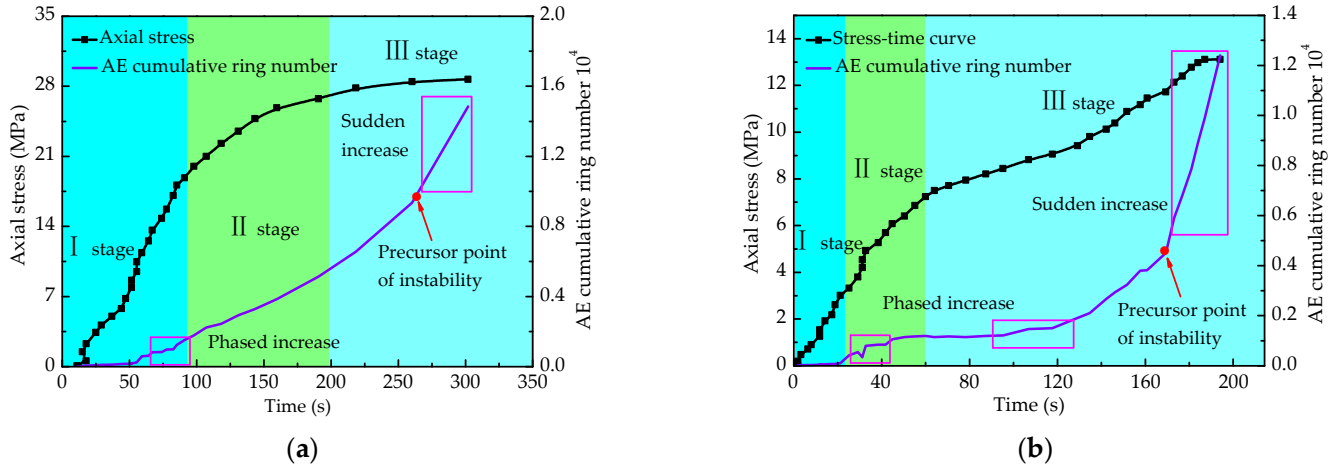

Figure 8. Evolution of AE cumulative ring number under parallel loading: (**a**) Gray samples; (**b**) Carbonaceous samples.

The slate sample is in the compaction stage and the primary cracks are compacted and closed, with almost no new fractures generated during the initial stage of axial stress loading. The AE activity is relatively weak, and the AE cumulative ring number has no significant increase, that is, the AE activity is in a quiet stage [25]. The existence of a weak surface in a slate sample causes local micro-fracture during the initial loading process, in turn, causes the AE activity to increase, and the AE cumulative ring number-time curve increases briefly. The vertical loading causes the principal stress to be in series with slate bedding plane (Figure 7), the compression process of slate sample is longer, and the increase in the AE cumulative ring number is small. The loading stress induces early tensile fracture of the weak surfaces and early initiation and expansion of internal fissures under parallel loading (Figure 8). A local microscopic fracture surface is formed, and the AE frequency and intensity are greater than that for vertical loading.

The slate sample gradually enters the elastic deformation stage due to the internal fissures being compressed. The layered weak surfaces inside the slate sample induce new

clefts to appear rapidly, the AE activity is slightly enhanced, and the AE cumulative ring number develops slowly, which is different from the AE characteristics of intact rock. The differences in loading directions lead to differences in AE characteristics at the elastic deformation stage. Fracture and slip of local weak layers cause the initiation of new cracks, and the drop in stress induces a stepwise increase in the AE cumulative ring number. In particular, when vertical loading is applied, the rock formation undergoes phased oblique shear rupture, leading to phased AE activities. The AE cumulative ring number shows a sudden, local increase around 600 s, 750 s, and 800 s as shown in Figure 7a. The AE cumulative ring number has a local sudden increase of around 650 s, as shown in Figure 7b.

When the slate sample undergoes plastic deformation, the uncoordinated deformation between the slate rock layers is relatively active, leading to the initiation, expansion, and convergence of new internal fractures and brittle bursts appear during the formation of macro-cracks or micro-cracks. The AE activity at this stage is significantly enhanced; the AE cumulative ring number appears to increase suddenly, then it reaches a maximum value immediately thereafter. The cumulative values of the AE ring number for the slate sample are 23,048.75, 18,085, 14845, and 12,395. This shows that internal cracks penetrate rapidly; the microscopic cracks rapidly expand into macroscopic cracks, and the rock stability decreases sharply, until it ruptures. After the slate rock is loaded to the peak stress, the strain gauges break rapidly, thus failing to acquire the post-peak stress and strain data. Therefore, this paper does not include the development trend of the post-peak AE cumulative ring number curve. Figure 8 shows that the AE intensity of the gray samples is higher than that of the cinerous samples, regardless of the loading being vertical or parallel. The load-bearing capacity of slate rock near the peak stress reaches a maximum value, the strain energy is released rapidly, the macro cracks are gradually formed, and the AE activity reaches the peak period. Therefore, a sudden increase in AE cumulative ring number near the peak stress indicates instability and rupture, which can be used as precursor information for rock mass rupture. Based on this, Figures 7 and 8 show the precursor onset points of instability of different types of slate, and the AE cumulative ring numbers are 1.12×10^4 (1055.26 s), 0.79×10^4 (840.82 s), 0.96×10^4 (264.24 s), and 0.45×10^4 (176.82 s).

3.4. Failure Characteristics

3.4.1. Macro-Fracture Mode Characteristics

The failure mode and fracture shapes reflect the failure mechanisms directly for different loading conditions. It not only directly reflects the stress distribution during the loading process but also indirectly reflects the effects of differences in the degree of development, mineral composition, and internal defects of the internal structure on the overall strength. In particular, for slate rock with plate-like structures, in a weathered state, there are significant anisotropic characteristics in the rock interior. Its complex stress state can easily lead to floor heave and slabbing failure in roadways.

To study the failure mode and fracture characteristics, Figures 9–12 show the fracture distribution under vertical and parallel loading. Combined with the results of uniaxial compression tests, the brittleness and ductility of rock samples can be divided by the axial peak strain [29]. For a uniaxial peak strain of less than 1%, the rock samples show brittle failure. For a uniaxial peak strain in the range of 1% to 5%, the rock samples show brittle and ductile failure. For a uniaxial peak strain greater than 5%, the rock samples show ductile failure. Tables 1 and 2 show that when the axial stress is perpendicular to the slate structure, the peak strains of the gray samples and the carbonaceous samples are 1.24−2.97‰, and 1.09−2.05‰, respectively. When the axial stress is loaded parallel to the slate structure, the peak strength of gray samples and the carbonaceous samples are 3.27−6.26‰, and 1.29−1.58‰, respectively. Therefore, the peak strains of gray and carbonaceous samples are less than 1.00%, and the slate rock show brittle failure.

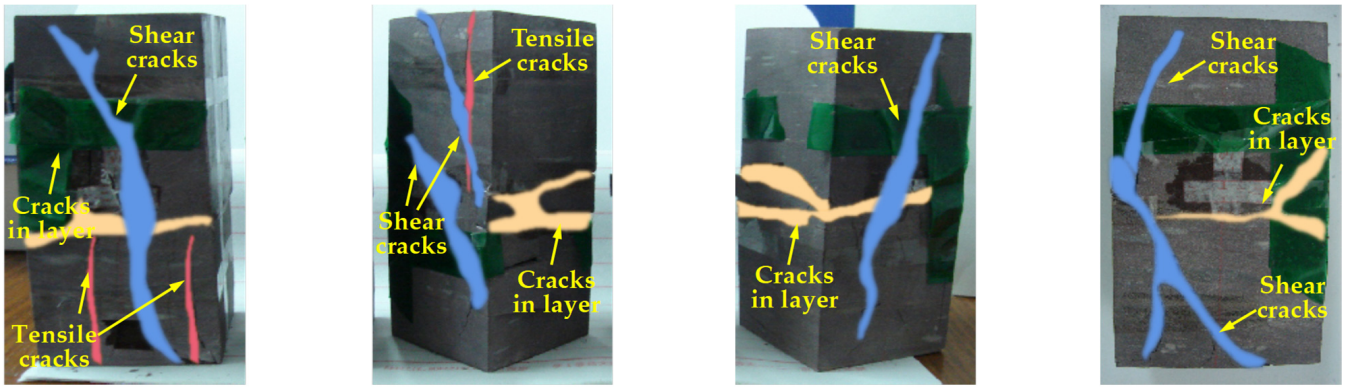

Figure 9. Fracture distribution of gray samples under vertical loading: (**a**) No. 1 sample; (**b**) No. 2 sample; (**c**) No. 3 sample; (**d**) No. 4 sample.

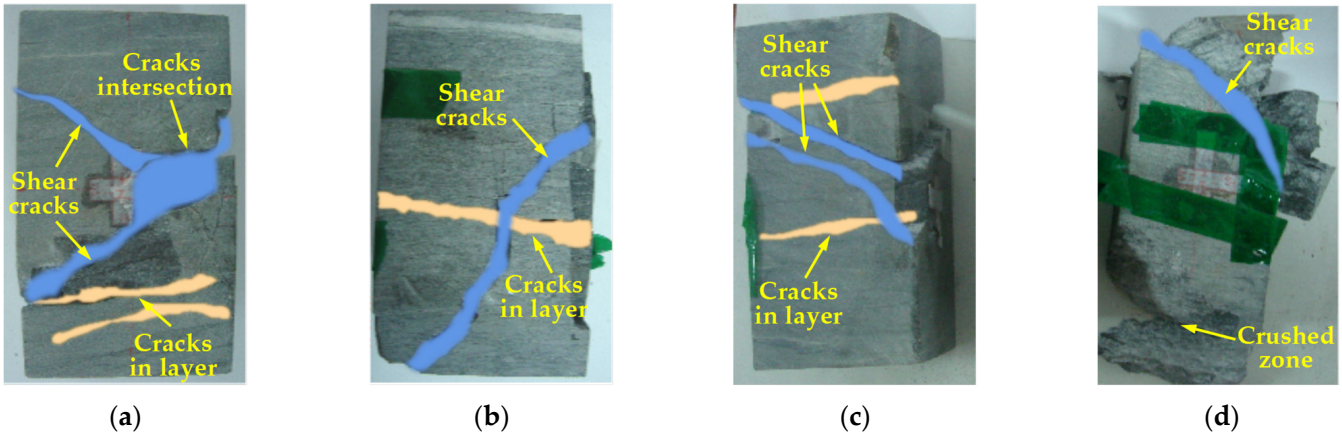

Figure 10. Fracture distribution of carbonaceous samples under vertical loading: (**a**) No. 1 sample; (**b**) No. 2 sample; (**c**) No. 3 sample; (**d**) No. 4 sample.

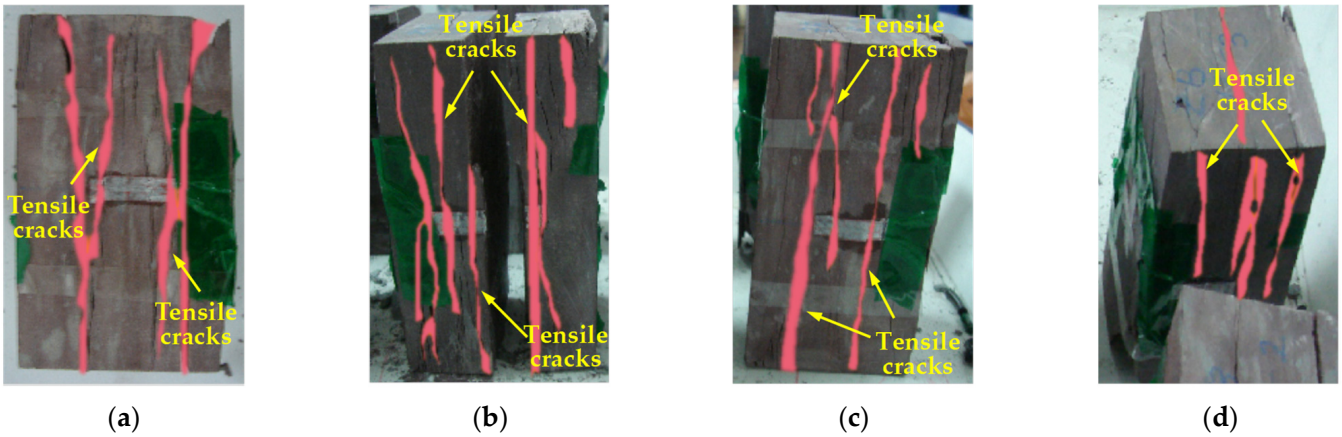

Figure 11. Fracture distribution of gray samples under parallel loading: (**a**) No. 1 sample; (**b**) No. 2 sample; (**c**) No. 3 sample; (**d**) No. 4 sample.

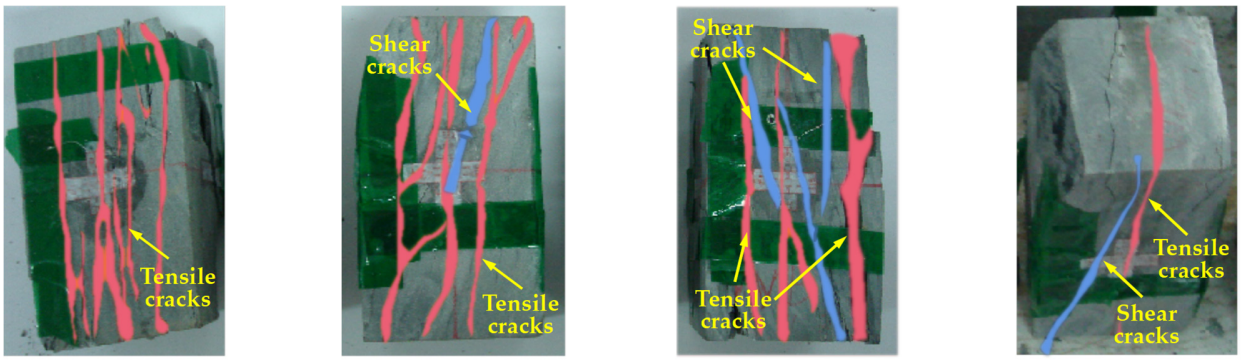

(**a**) (**b**) (**c**) (**d**)

Figure 12. Fracture distribution of carbonaceous samples under parallel loading: (**a**) No. 1 sample; (**b**) No. 2 sample; (**c**) No. 3 sample; (**d**) No. 4 sample.

Figures 9 and 10 show that when the axial stress is loaded perpendicular to the slate structure, the failure modes of the gray and carbonaceous samples are oblique shear fracture, and shear fractures on the surface of the slate sample were observed. Compared with the carbonaceous samples, when the gray samples undergo shear failure, they are also prone to bursting and ejecting rock blocks, forming missing areas and which aggravate the fragmentation of the slate sample surface. The broken areas are mostly located near the primary shear fractures, as shown in Figure 9a. This is because the quartz content in gray slate is significantly more than that in carbonaceous slate, and the increase of quartz minerals aggravates brittle deformations of rock samples [29–31]. Due to the differences in the mineral content of rock samples, only one main shear fracture appears on the surface of the gray samples, and the fracture length is about 70.00–75.86 mm. There are 2 to 3 microfractures in the shear fracture and the fragmented edge of the carbonaceous samples, and the angle between microfracture and shear fracture is 38°−45°. The appearance of broken areas and microfractures aggravate the rate of dilation speed of the slate samples. It should be pointed out that the fragmented area of the No.4 carbonaceous sample is a fragment formed by the rock sample falling and hitting the ground after shearing failure, as shown in Figure 10b.

Figures 11 and 12 show the fracture distributions of gray and carbonaceous samples under parallel loading, respectively. They show that axial stress has a significant impact on failure modes. Figure 11 shows that the fracture mode of the gray samples is mainly splitting failure, and segregation appears in the slate structures under parallel loading. The direction of the main fragments formed is parallel to the loading stress, and the tension causes the slate sample to expand towards both sides. There are 1–2 splitting fractures on the surfaces of the gray samples, and 2–3 expansive microfractures near the center surfaces. The length of the microfracture is about 30–50 mm. The direction of the expansive microfracture is approximately parallel to splitting fracture. As presented in Figure 12, the carbonaceous samples also show splitting failure. There are shear fractures in the No.2 carbonaceous sample and the No.3 carbonaceous sample, and the extent of penetration of expansion microfractures on the surfaces of carbonaceous samples is not evident. The microfracture length is about 30–45 mm, and its angle with the splitting fracture is 10°−30°. Compared with the gray samples, segregation in the slate structures of carbonaceous samples is not observed.

3.4.2. Micro-Cracks and Fracture Characteristics

The macroscopic fracture mode of slate samples shows that the slate structural surface and principal stress are in a state of series interaction under vertical loading, and the cracks formed by the progressive fracture dominate the oblique shear fracture. The uneven stress adjustment and structural deformation between the slate structural surfaces under compressive stress cause local tensile fractures, and the slate surface is mainly composed

of macroscopic oblique shear cracks along with local tension cracks. The slate structural surface and principal stress show parallel interaction during parallel loading, leading to the lateral deformation of longitudinal, weak structural surfaces and causing tension cracks. Irreversible deformation accumulates rapidly, leading to tensile fracture and the macroscopic cracks formed on the surface are mainly tensile cracks and seldomly oblique shear cracks. The rapid accumulation of irreversible deformation leads to tensile fracture, resulting in the formation of macroscopic cracks on the surface that are mainly tensile, while oblique shear cracks are rarely seen.

Figure 13 shows the micro-cracks and fracture characteristics of slate samples under vertical loading. The microscopic fracture morphology of gray samples and cinerous samples have similar characteristics under vertical loading. The brittle fracture of the mineral structure is caused by oblique shear and tensile fracture effects; the fracture sections formed are relatively smooth as shown in Figure 13a,b. The microscopic cracks extend along the interface of the crystal, and the smooth sections are accompanied by the penetrating cracks or fissure groups as shown in Figure 13c,d. The disturbance of the principal stress induces bedrock fracture and also causes the cement and fractured mineral crystals to be scattered on the fracture surface, forming microscopic features such as pores between cement bodies, cracks between crystals, and caves. Figure 13a,b show a large number of smooth micro-fractures and micro-cracks on the fracture surface and stepped smooth fractures with approximately parallel port surfaces. Figure 13c,d show stepped smooth fractures and microscopic group cracks that appear in smooth fractures. The group of cracks derived from the crystal surface indicates complex intergranular mechanical effects. In addition, the broken mineral crystals are scattered near the stepped fractures formed by the local shear effect.

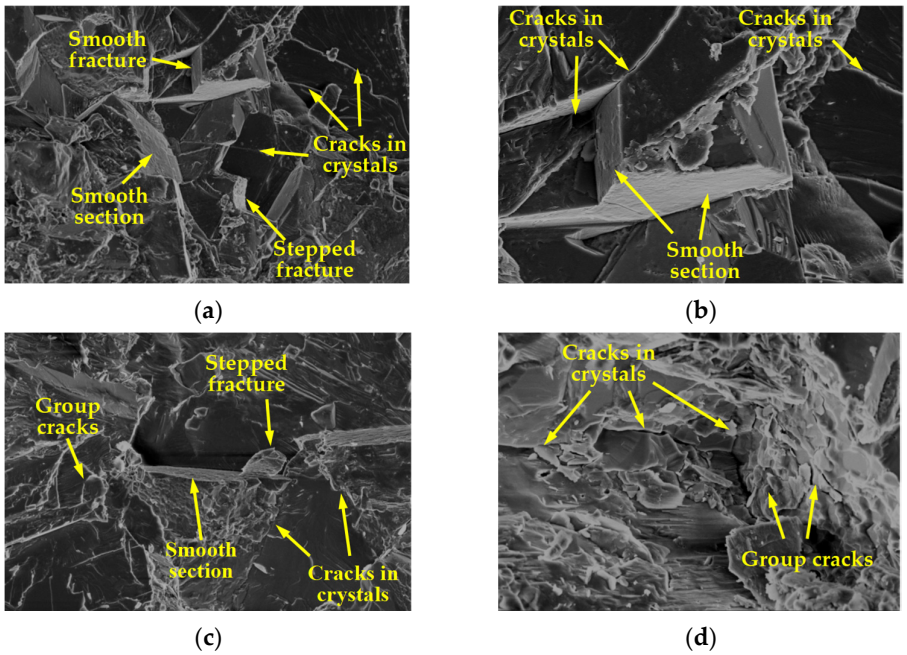

Figure 13. Micro-cracks and fracture characteristics under vertical loading: (**a**) Gray sample (2000×); (**b**) Gray sample (5000×); (**c**) Carbonaceous Sample (2000×); (**d**) Carbonaceous Sample (5000×).

The reason for the above is that the principal stress first causes the compression and deformation of the weak surface of the slate, leading to uneven stress distribution, following which stress concentration occurs. The gradual fracture of the layered structure leads to tensile cracks of microscopic mineral crystals, forming transcrystalline cracks and prismatic steeped fractures. Also, the layered structure effect exacerbates the tendency of local structural surfaces towards slip and shear deformation. The effects of slip friction, rubbing, and tearing aggravate the peeling of cement, mineral particles, and fractured

mineral crystals. In addition, the degree of cementation of the slate structural surface is affected by the size of the mineral particles and the characteristics of the bedding structure. The fracture characteristics are not simply affected by compression deformation and oblique shearing slip but are also related to the stress distribution between mineral crystals and cement, and the process of structural adjustment [29].

Figure 14 shows the micro-cracks and fracture characteristics under parallel loading. Compared with slate samples under vertical loading, slate samples under parallel loading primarily show a tensile fracture, and the fractured sections have a lower roughness. The scattered fractures and sections are smooth without protrusions or transcrystalline cracks. This is mainly due to the tensile fracture of weak surface structures due to the principal stress disturbance, and the fracture surface formed after the cement cracking dominates the slate fracture trend [32,33], and only local mineral crystals have a tensile fracture. Structural stress adjustment in the gradual intersection of internal cracks leads to mechanical effects such as friction and tearing on the macroscopic fracture surface, which in turn, causes tensile and tearing fractures, clustered tensile fractures, concave tensile fractures, friction scratches, or intergranular cracks. Figure 14 shows that the principal stress causes microscopic penetration cracks with no smooth fractures. The tearing and tensioning effects on the weak surface of slate are caused by transverse tension which results in layered fractures (Figure 14b) and produces smooth sections without micro-cracks (Figure 14c,d). This is significantly different from the micro-cracks and fracture characteristics under vertical loading. An analysis of the mechanism of action indicates that when the principal stress is parallel to the weak structure surface, the rock pillar causes the stress interaction between mineral crystals due to the compression rod effect [34,35], following which the damage degree of slate is significantly improved. The differences in the load-bearing strength of mineral crystals cause stronger mineral crystals to wedge into the lower-strength structural layer, resulting in cracks in surrounding rock formations, which increases structural damage. The wedging action of crystals leads to general convergence through the cracks and decomposition of the mineral structure. The degree of damage is closely related to the cohesive force in mineral crystals and the cementation strength between the mineral crystal and cement. Therefore, microstructural changes are the cause of the deterioration of the mechanical properties of slate.

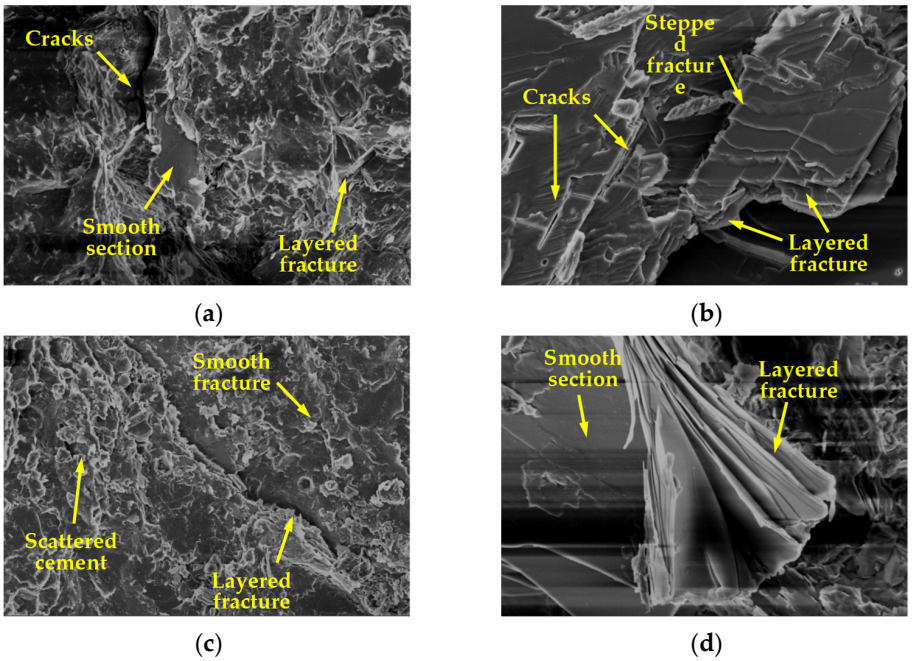

Figure 14. Micro-cracks and fracture characteristics under parallel loading: (**a**) Gray sample (2000×); (**b**) Gray sample (5000×); (**c**) Carbonaceous sample (2000×); (**d**) Carbonaceous sample (5000×).

The fracture morphology and micro-fracture characteristics of slate samples indicate that slate microstructure has three types of microstructure fracture modes; intergranular fractures (cracks appear on the edge of the crystal and cement), transgranular fractures (stress concentration causes cracks to pass through the crystal), and intergranular-transgranular composite fractures (cracks gradually expand through the cement and crystal structure), which is consistent with shale micromechanical features [36–40]. There are differences in fracture smoothness, fracture area, and the presence of micro-cracks between vertical and parallel loading modes.

4. Conclusions

The direction of stress loading and the bedding effect significantly impact strain and mechanical parameters. The deformation goes through compaction, elastic, damage accumulation, and failure stages, and there are significant differences in strain paths. The weak structural plane of the bedding controls the overall deformation when loaded perpendicular to a weak surface structure, showing a significant plastic deformation. The rock pillar effect weakens the axial deformation under parallel loading. The mechanical properties of grey and carbonaceous slate have significant discrete features.

The variation coefficient of gray slate samples is characterized by the peak stress, expansion stress, and elastic modulus of 1.22, 1.35 and 0.69, respectively. The variation coefficient of the carbonaceous slate samples is characterized by the peak stress, expansion stress, and elastic modulus of 1.46, 1.38, and 0.71, respectively. The uniaxial compression mechanical properties of gray and cinerous slate under different loading conditions have significant and discrete characteristics. The variations of the carbonaceous samples are greater than those of the gray samples, and they show complex fracture patterns and uneven fracture patterns in macroscopic views. The discrete degree (K) is significantly related to the direction of stress loading and different types of slate structures.

The AE response intensity of slate samples is related to the loading mode and slate type. A sudden increase in the AE cumulative ring number near the peak stress indicates instability and rupture, which can be used as a precursor of rock rupture. The failure patterns and fracture characteristics are significantly related to the slate structure. Slate samples under vertical loading and parallel loading conditions are dominated by shear fracture and tensile fracture, respectively. The peak strains of gray slate and cinerous slate are less than 1.00%, resulting in brittle failure. The SEM tests indicate that slate samples under parallel loading primarily incur tensile fracture compared with slate samples under vertical loading, and the fractured section has a smaller roughness; the scattered fractures and sections are smooth without protrusions or transcrystalline cracks.

Author Contributions: Methodology, Z.Z.; Writing—original draft, Z.Z., Y.C., Z.S. and X.Y.; writing—review & editing, Y.C. and Z.S. All authors have read and agreed to the published version of the manuscript.

Funding: This work was financially supported by the Guangxi Natural Science Foundation general project (Grant No. 2022GXNSFAA035582), National Natural Science Foundation of China (Grant No. 52178393), Innovation Capacity Support Plan of Shaanxi Province (Grant No. 2020TD−005), Talent Project of Beibu Gulf University (Grant No. KYQD2132017), and Science and Technology Innovation Project of China Railway Construction Bridge Engineering Bureau Group Co., Ltd. (Grant No. DQJ-2020-B07).

Institutional Review Board Statement: Not applicable.

Informed Consent Statement: Not applicable.

Data Availability Statement: The data used to support the findings of this study are available from the corresponding author upon request.

Conflicts of Interest: The authors declare no conflict of interest.

References

1. Zhu, C.; He, M.C.; Zhang, X.H.; Tao, Z.G.; Yin, Q.; Li, L.F. Nonlinear mechanical model of constant resistance and large deformation bolt and influence parameters analysis of constant resistance behavior. *Rock Soil Mech.* **2021**, *42*, 1911–1924. [CrossRef]
2. Zhu, C.; He, M.C.; Jiang, B.; Qin, X.Z.; Yin, Q.; Zhou, Y. Numerical investigation on the fatigue failure characteristics of water-bearing sandstone under cyclic loading. *J. Mt. Sci.* **2021**, *18*, 3348–3365. [CrossRef]
3. Wu, K.; Shao, Z.; Qin, S.; Zhao, N.N.; Chu, Z. An improved non-linear creep model for rock applied to tunnel displacement prediction. *Int. J. Appl. Mech.* **2021**, *13*, 2150094. [CrossRef]
4. Wu, K.; Shao, Z.; Qin, S.; Wei, W.; Chu, Z.F. A critical review on the performance of yielding supports in squeezing tunnels. *Tunn. Undergr. Space Technol.* **2021**, *115*, 103815. [CrossRef]
5. Cheng, Y.; Song, Z.P.; Yang, T.T.; Han, J.J.; Wang, B.W.; Zhang, Z.K. Investigating the aging damage evolution characteristics of layered hard sandstone using digital image correlation. *Constr. Build. Mater.* **2022**, *335*, 128838. [CrossRef]
6. Wu, K.; Shao, Z.S.; Sharifzadeh, M.; Chu, Z.F.; Qin, S. Analytical approach to estimating the influence of shotcrete hardening property on tunnel response. *J. Eng. Mech.* **2022**, *148*, 4021127. [CrossRef]
7. Wu, K.; Shao, Z.; Sharifzadeh, M.; Hong, S.; Qin, S. Analytical computation of support characteristic curve for circumferential yielding lining in tunnel design. *J. Rock Mech. Geotech. Eng.* **2022**, *14*, 144–152. [CrossRef]
8. Zhou, G.N.; Yang, T.T.; Sun, Z.; Li, H.; Cheng, Y.; Song, Z.P.; Han, J.J. Investigation of quantitative evaluation method and engineering application of shallow buried tunnel face stability. *Appl. Sci.* **2022**, *12*, 6656. [CrossRef]
9. Yang, L.F.; Shi, K.X.; Wang, C.M.; Wu, B.; Du, B.; Chen, J.Y.; Xia, J.S.; Chen, J. Ore genesis of the Jinman copper deposit in the Lanping Basin, Sanjiang Orogen: Constraints by copper and sulfur isotopes. *Acta Petrol. Sin.* **2016**, *32*, 2392–2406.
10. Tian, X.X.; Song, Z.P.; Zhang, Y.W. Monitoring and reinforcement of landslide induced by tunnel excavation: A case study from Xiamaixi tunnel. *Tunn. Undergr. Space Technol.* **2020**, *110*, 103796. [CrossRef]
11. Tian, X.X.; Song, Z.P.; Wang, H.Z.; Zhang, Y.W.; Wang, J.B. Evolution characteristics of the surrounding rock pressure and construction techniques: A case study from Taoshuping tunnel. *Tunn. Undergr. Space Technol.* **2022**, *125*, 104522. [CrossRef]
12. Vervoort, A.; Min, K.B.; Konietzky, H.; Cho, J.W.; Debecker, B.; Dinh, Q.D.; Frühwirt, T.; Tavallali, A. Failure of transersely isotropic rock under Brazilian test conditions. *Int. J. Rock Mech. Min. Sci.* **2014**, *70*, 343–352. [CrossRef]
13. Dan, D.Q.; Konietzky, H. Numerical simulations and interpretations of Brazilian tensile tests on transversely isotropic rocks. *Int. J. Rock Mech. Min. Sci.* **2014**, *7*, 53–63. [CrossRef]
14. Zhang, P.; Yang, C.H.; Wang, H.; Guo, Y.T.; Xu, F.; Hou, Z.K. Stress-strain characteristics and anisotropy energy of shale under uniaxial compression. *Rock Soil Mech.* **2018**, *39*, 2106–2114. [CrossRef]
15. Wang, C.C.; Li, J.T.; Lin, H.; Liao, J.; Wang, P.X.; Wang, S.Q. Anisotropic mechanical characteristics of slate in uniaxial compression. *J. Cent. South Univ.* **2016**, *47*, 3759–3764. [CrossRef]
16. Li, Z.G.; Xu, G.L.; Huang, P.; Zhao, X.; Fu, Y.P. Mechanical and anisotropic properties of silty slates. *Rock Soil Mech.* **2018**, *39*, 1737–1746. [CrossRef]
17. Hou, Z.Q.; Wang, Y.; Liu, D.Q.; Li, C.H. Investigation of the anisotropic mechanical behaviors and energy evolution during uniaxial deformation of interbedded marble. *J. Min. Saf. Eng.* **2019**, *36*, 794–804. [CrossRef]
18. Fan, X.; Kulatilake, P.H.S.W.; Chen, X.; Cao, P. Crack initiation stress and strain of jointed rock containing multi-cracks under uniaxial compressive loading: A particle flow code approach. *J. Cent. South Univ.* **2015**, *22*, 638–645. [CrossRef]
19. Akbarimehr, D.; Eslami, A.; Aflaki, E. Geotechnical behaviour of clay soil mixed with rubber waste. *J. Clean. Prod.* **2020**, *271*, 122632. [CrossRef]
20. Fan, S.Y.; Song, Z.P.; Zhang, Y.W.; Liu, N.F. Case study of the effect of rainfall infiltration on a tunnel underlying the roadbed slope with weak inter-layer. *KSCE J. Civ. Eng.* **2020**, *24*, 1607–1619. [CrossRef]
21. Fan, S.Y.; Song, Z.P.; Xu, T.; Wang, K.M.; Zhang, Y.W. Tunnel deformation and stress response under the bilateral foundation pit construction—A case study. *Arch. Civ. Mech. Eng.* **2021**, *109*, 109. [CrossRef]
22. Li, G.T.; Qiao, D.P.; Yu, X.B.; Wang, J. Experimental investigation on the tensile deformation as a result of the brazilian test for the rocks of Dahongshan copper mine. *J. Saf. Environ.* **2017**, *17*, 463–467. [CrossRef]
23. Song, B.; Cao, Y. Stability criterion of surrounding rock in roadway under blasting vibration load based on wavelet energy. *Rock Soil Mech.* **2013**, *34*, 234–240. [CrossRef]
24. Song, Z.P.; Cheng, Y.; Tian, X.X.; Wang, J.B.; Yang, T.T. Mechanical properties of limestone from Maixi tunnel under hydro-mechanical coupling. *Arab. J. Geosci.* **2020**, *13*, 402. [CrossRef]
25. Song, Z.P.; Cheng, Y.; Yang, T.T.; Huo, R.K.; Wang, J.B.; Liu, X.R.; Zhou, G.N. Analysis of compression failure and acoustic emission characteristics of limestone under permeability-stress coupling. *Rock Soil Mech.* **2019**, *44*, 2751–2759. [CrossRef]
26. Li, G.; Hu, Y.; Tian, S.M. Analysis of deformation control mechanism of prestressed anchor on jointed soft rock in large cross-section tunnel. *Bull. Eng. Geol. Environ.* **2021**, *80*, 9089–9103. [CrossRef]
27. Lin, B.; Zhang, F.; Feng, D.C.; Ma, H.Y.; Feng, X. Experimental investigation on strain rate effects of saturated clay subjected to freeze-thaw cycles. *Rock Soil Mech.* **2017**, *38*, 2007–2014. [CrossRef]
28. Cheng, Y.; Song, Z.P.; Huo, R.K.; Yang, T.T.; Wang, J.B. Study on the effect of pore-water pressure on Felicity effect of acoustic emission in limestone under graded cyclic loading. *J. Basic Sci. Eng.* **2022**, *30*, 361–373. [CrossRef]
29. Wang, Y.P.; Liu, X.J.; Liang, L.X. Influences of bedding planes on mechanical properties and prediction method of brittleness index in shale. *Lithol. Reserv.* **2018**, *30*, 149–160. [CrossRef]

30. Cheng, Y.; Song, Z.P.; Jin, J.F.; Wang, T.; Yang, T.T. Waveform characterisation and energy dissipation of stress wave based on modified SHPB tests. *Geomech. Eng.* **2020**, *22*, 187–196. [CrossRef]
31. Cheng, Y.; Song, Z.P.; Chang, X.X.; Wang, T. Energy evolution principles of shock-wave in sandstone under unloading stress. *KSCE J. Civ. Eng.* **2020**, *24*, 2912–2922. [CrossRef]
32. Gao, M.Z.; Xie, J.; Gao, Y.N.; Wang, W.Y.; Li, C.; Yang, B.G.; Liu, J.J.; Xie, H.P. Mechanical behavior of coal under different mining rates: A case study from laboratory experiments to field testing. *Int. J. Min. Sci. Technol.* **2021**, *31*, 825–841. [CrossRef]
33. Gao, M.Z.; Hao, H.C.; Xue, S.N.; Lu, T.; Cui, P.F.; Gao, Y.N.; Xie, J.; Yang, B.G.; Xie, H.P. Discing behavior and mechanism of cores extracted from Songke-2 well at depths below 4500 m. *Int. J. Min. Sci. Technol.* **2022**, *149*, 104976. [CrossRef]
34. Cheng, Y.; Song, Z.P.; Song, W.X.; Li, S.G.; Yang, T.T.; Zhang, Z.K.; Wang, T.; Wang, K.S. Strain performance and fracture response characteristics of hard rock under cyclic loading. *Geomech. Eng.* **2021**, *26*, 551–563. [CrossRef]
35. Dou, Z.; Tang, S.X.; Zhang, X.Y.; Liu, R.C.; Zhuang, C.; Wang, J.G.; Zhou, Z.F. Influence of shear displacement on fluid flow and solute transport in a 3D rough fracture. *Lithosphere-US* **2021**, *2021*, 1569736. [CrossRef]
36. Chai, B.; Tong, J.; Jiang, B.; Yin, K.L. How does the water-rock interaction of marly rocks affect its mechanical properties in the Three Gorges reservoir area, China. *Environ. Earth Sci.* **2014**, *72*, 2797–2810. [CrossRef]
37. Chen, D.H.; Chen, H.E.; Zhang, W.; Lou, J.Q.; Shan, B. An analytical solution of equivalent elastic modulus considering confining stress and its variables sensitivity analysis for fractured rock masses. *J. Rock Mech. Geotech. Eng.* **2021**, *14*, 825–836. [CrossRef]
38. Wang, Z.Q.; Yan, E.C.; Liu, Y.X.; Wang, Z.J. Anisotropic properties of deformation parameters and its mechanism of Wudang group schist. *Rock Soil Mech.* **2015**, *35*, 1317–1322+1328.
39. Liu, N.F.; Li, N.; Xu, C.B.; Li, G.F.; Song, Z.P.; Yang, M. Mechanism of secondary lining cracking and its simulation for the dugongling tunnel. *Rock Mech. Rock Eng.* **2020**, *53*, 4539–4558. [CrossRef]
40. Liu, N.F.; Li, N.; Li, G.F.; Song, Z.P.; Wang, S.J. Method for evaluating the equivalent thermal conductivity of a freezing rock mass containing systematic fractures. *Rock Mech. Rock Eng.* **2022**, *2022*, 1–23. [CrossRef]